6.0 PROPAGATION AND ADAPTIVE OPTICS

Steven Fiorino and Jack E.McCrae
Air Force Institute of Technology (AFIT) – Wright-Patterson AFB, OH
USA
steven.fiorino@afit.edu, jack.mccrae@afit.edu

Virtually all the atmospheric effects on laser weapon systems can be traced to three atmospheric phenomena: absorption, scattering, and turbulent motions. All three phenomena have some degree of spectral wavelength dependency, are interrelated through the complex index of refraction and have direct deleterious effects on laser propagation. Absorption additionally can create non-linear thermal blooming effects for High Energy Laser (HEL) propagation. [6.1]

6.1 Propagation

6.1.1 Absorption, Scattering, & Thermal Blooming

Absorption and scattering are often combined and referred to as extinction. Extinction is of paramount importance in calculating the overall loss of laser energy along a path as the equation for transmission requires the sum of absorption and scattering for all gases, aerosols, and hydrometeors the beam encounters. However, the individual resultant effects of absorption and scattering on laser propagation are markedly different, so they will be treated separately here. [6.1]

Absorption is most simply described as the capture of photons at one energy level with a resulting re-emission of photons at another, lower, energy level. Eventually the electronic, vibrational, and rotational transitions that occur within the absorbing molecules result in molecular collisions that in turn cause additional translational kinetic motions of the molecules. Thus, the absorbing medium usually gains thermal energy—it gets hotter. [6.1]

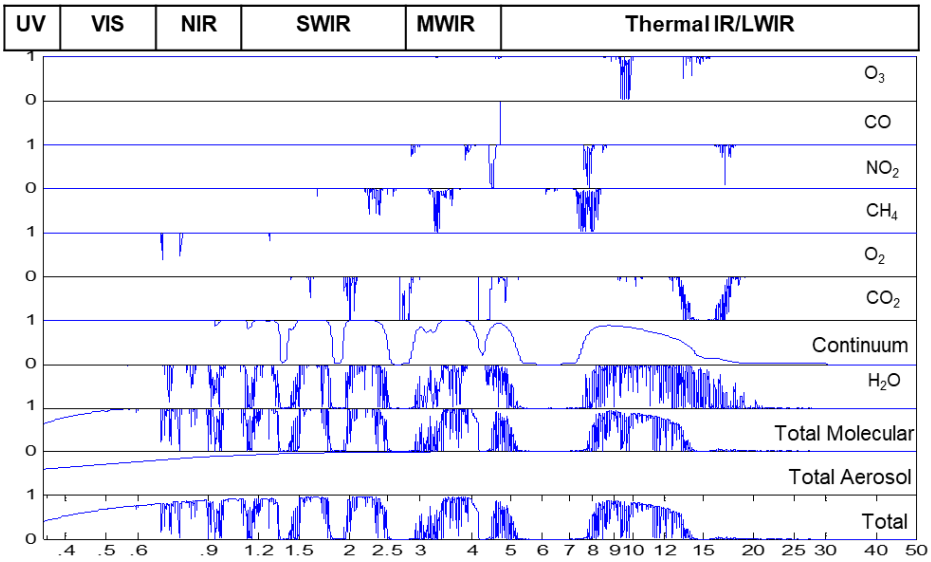

Figure 6-1: Zenith transmission of the cloud- and aerosol-free atmosphere for typical mid-latitude summer conditions. Each upper panel depicts the absorption contribution due to a single atmospheric constituent; the bottom panel depicts the combined effects of all constituents. Molecular scattering is included. (Derived from Air Force Institute of Technology, *Laser Environmental Effects Definition and Reference*, software package, [6.2]).

Interestingly, the primary absorbers of electromagnetic energy in the atmosphere are not the largest constituents. In fact, it is the trace gases and water vapor that play the most significant role in atmospheric absorption, as illustrated in Figure 6-1. Figure 6-1 shows the total zenith transmittance for a summer midlatitude atmosphere (bottom graph) and for seven of the primary absorbing gases. Water vapor is the single most important absorber across the part of the spectrum shown, given that its plot is most similar to the total plot. Carbon dioxide, ozone and oxygen are also important. Each of the gases' contributions to the overall transmission can be calculated with

$$T_{abs} = \frac{I_t(\lambda)}{I_o(\lambda)} = e^{-\sigma_{abs}(\lambda) N z}$$

where σ_{abs} is the absorption cross-sectional area (m^2), N is the absorber number concentration (m^{-3}), and $\alpha_a = \sigma_{abs} N$.

Water vapor's importance as an absorbing gas continues beyond the $\lambda = 50$ μm limit shown in Figure 6-1. Figure 6-2 extends the zenith transmission plot into the microwave and radio frequencies, and includes the spectral locations of several common lasers and laser weapon systems. Note that water vapor is the primary absorber at the most common laser wavelengths. Thus the seasonal, time-of-day, horizontal, and vertical variability of atmospheric water vapor will play a critical role in the successful employment of future laser weapon systems.

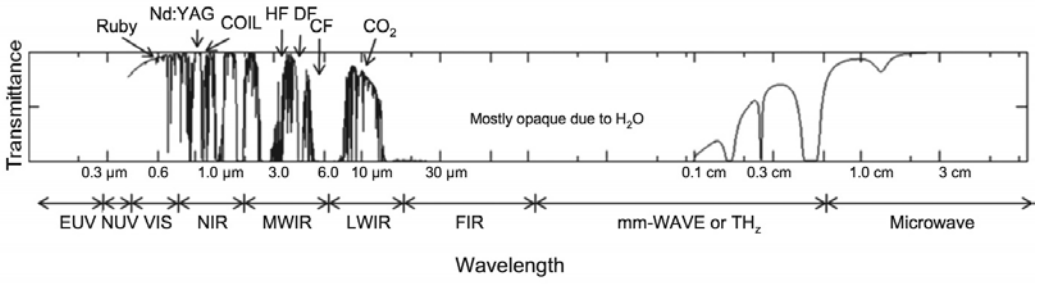

Figure 6-2: Total zenith transmission plot from UV to microwave with specific spectral bands labelled and typical laser wavelengths noted. Molecular scattering effects are included. (Derived from Air Force Institute of Technology, *Laser Environmental Effects Definition and Reference*, software package, [6.2]).

In addition to directly reducing the transmission of laser energy delivered along a path, absorption also causes heating of the air within the beam. This particularly affects the propagation of high energy beams as there are orders of magnitude more photons concentrated into a focused HEL beam than with a low power or highly diverging beam. This effect is called thermal blooming. Thermal blooming is defined as the effect that occurs when an intense laser beam is passed through an absorbing medium, causing the absorbed energy to produce density changes that alter the index of refraction of the air and the intensity distribution of the beam and shift it away from the intended direction of propagation. [6.1]

The primary initial effects of thermal blooming are to bend the laser beam toward the cooler, denser air. The classic crescent spot shape due to thermal blooming is clearly evident in the wave optics plot shown in Figure 6-3. This demonstrates how the intensity distribution is spread due the gradient in the index of refraction toward the air being brought into the beam by the wind or the movement (slewing) of the beam. [6.1]

Thermal blooming can be mathematically described using the thermal blooming distortion number:

$$N_D = -\frac{4\sqrt{2}k\mathrm{P}}{\rho_0 C_p}\int_{path}\frac{\alpha(z)\mathrm{T}(z)n_T(z)}{V_{wind}(z)D(z)}dz \tag{6.1}$$

where z in this case is distance along the total slant path of the beam, R, $n_T = dn/dT = (n_0 - 1)/T$, $\alpha(z)$ is the absorption coefficient, $V_{wind}(z)$ is the effective wind speed perpendicular to the beam, P is the laser power, k is wavenumber, $D(z)$ is the beam diameter, T in italics is temperature, and T(z) is transmission at range z. Some researchers include a weighting function:

$$F(z) = \frac{1}{\sqrt{1+\left(\frac{1.25\lambda R}{D^2}\right)^2\left(\frac{z/R}{1-z/R}\right)^2}} \tag{6.2}$$

in the integral in Equation 6.1. Including this weighting function can compensate for the so-called "lever arm" effect that describes how absorption near the aperture causes more significant blooming distortion than absorption near the target. Note that D in Equation 6.2 is in this case the primary aperture diameter. [6.1]

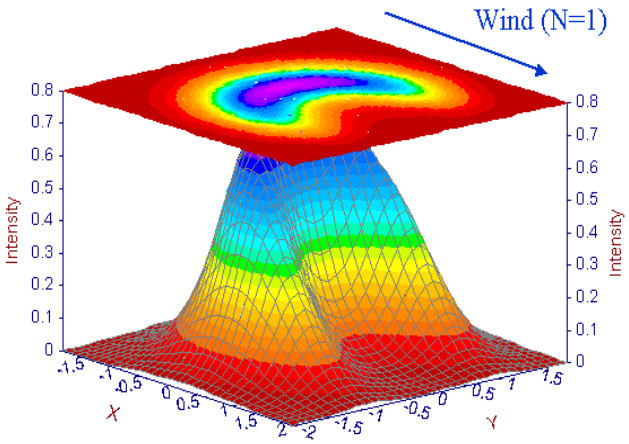

Figure 6-3: Thermal blooming produces an intensity pattern with a crescent shape turned into the wind direction.

While molecular (gaseous) absorption is the predominate cause of thermal blooming effects for HEL propagation, the absorption effects of aerosols and hydrometeors can be significant at times. In these cases, the absorption coefficients calculated for the aerosols and other particles are summed with the molecular absorption coefficients to obtain the total thermal blooming effect. Generally, however, the scattering effects of aerosols, water drops/droplets, and ice crystals are an order of magnitude greater than their absorption effects for laser wavelengths of 400 nm to 3 µm, and are of significantly greater concern than the absorption effects. [6.1]

Scattering by molecules, aerosols, and hydrometeors is important in laser propagation because it removes energy from the beam, reducing energy delivered to the target. Unlike absorption, however, scattering does not change the index of refraction of the beam; the scattered photons are elastically reflected in all directions according to a scattering phase function based on wavelength and scattering particle size. The energy lost to scattered photons can be of concern as it could possibly be detected and quantified off-axis, and/or exceed eye safety thresholds.

The effects of scattering on laser transmission can be calculated in a manner similar to that for absorption. Equation 6.3 can be used to obtain transmission values specifically caused by scattering:

$$T_{sca} = \frac{I_t(\lambda)}{I_o(\lambda)} = e^{-\alpha_s z} \tag{6.3}$$

where z is the transmission path and α_s is the scattering coefficient. Summing the scattering and absorption effects together allows for the calculation of $T = \frac{I_t}{I_o} = e^{-[\alpha_s(\lambda) + \sum_i \sigma^i_{abs}(\lambda) N_i] z}$ due to extinction, as expressed in Equation 6.4:

(6.4)

Scattering by molecules is significant for visible wavelengths, especially blue and violet, as is evidenced by the "Total Molecular" plot in Figure 6-1 where the transmission loss in the visible range is not due to absorption. Aerosol scattering is generally at least an order of magnitude greater than molecular scattering in the lower atmosphere, especially the boundary layer. This is true even for the visible wavelengths. However, in the absence of major volcanic eruptions, molecular scattering becomes the dominant scattering process again at altitudes above ~12 km for wavelengths up to 1.5 μm. [6.1]

Scattering by water-soluble aerosols, which are the most common type of boundary layer (BL) aerosols over much of the world's surface, is strongly modulated by relative humidity. Relative humidity is a measure of how saturated the air is, and it varies dramatically at the surface with diurnal temperature changes and with altitude in the BL. This results in a sharp increase in aerosol extinction, primarily due to scattering, near the top of the BL throughout much of the world under fair weather conditions. An example of this "spike" in aerosol extinction is illustrated in Figure 6-4, which shows both Lidar-measured and model-calculated aerosol extinction with height for Wright-Patterson AFB, OH in summer conditions. [6.1]

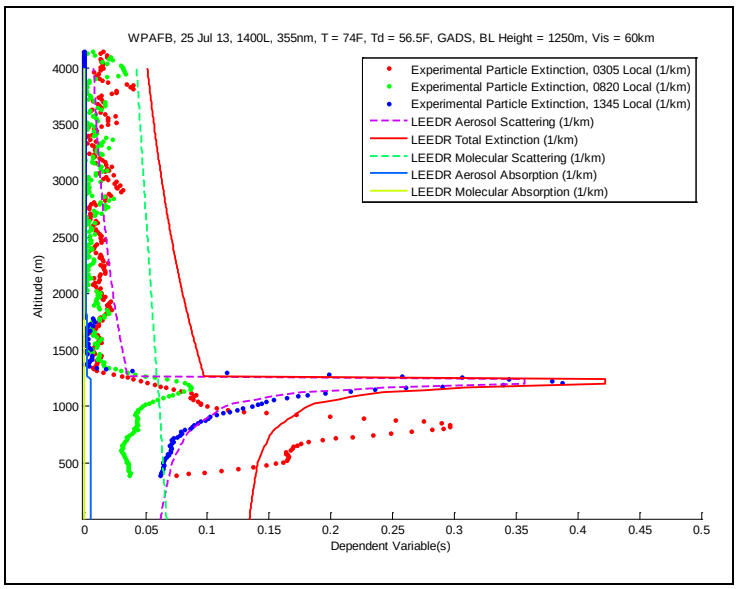

Figure 6-4: Absorption and scattering effects modelled by LEEDR compared with Raman lidar profile data points (dotted lines). LEEDR-modeled absorption and scattering effects for the same vertical path and surface aerosol concentration but applying an observed Dayton, Ohio, summer atmosphere at 1400 eastern daylight time 25 Jul 13 are shown with solid lines. [6.3]

In summary, absorption and scattering direct effects are broad spectrum, geographically, seasonally, and diurnally complex. Additionally, absorption can result in highly non-linear deleterious effects on HEL propagation in the form of thermal blooming. However, many of the effects can now be calculated very

rapidly—not only permitting enhanced scientific and engineering performance analysis, but also fast calculation for HEL weapon system mission planning and employment. [6.1]

6.1.2 Turbulence

Turbulence as it affects laser weapon systems is the result of vertical temperature differences (convection), wind shear, and inertial cascades of larger scale turbulences to smaller scales. The effects of turbulence on light propagation through the atmosphere have been long recognized. In the 1600's, Galileo's telescope and diffraction experiments by Huygens, Fresnel and others, allowed for the discovery that the image spread of stars was much broader (lower resolution) than expected from laboratory observations. In 1717, Newton first conjectured that this difference was due to the atmosphere. But it was not until the 1950's that little more than characterizing these effects-versus understanding-was accomplished. In 1958, Rosch's experiments with short exposure images produced his "bunch of grapes" theory. Soon thereafter in 1961, Kolmogorov published his treatise on spatial statistics of turbulent flow, and Tatarskii used Kolmogorov's model to develop his theory of electromagnetic wave propagation through turbulent media. Then in 1966, Fried employed Tatarskii's results to explain the difference between short and long exposure imagery and derived a single parameter, r_0, for describing the effects of turbulence on resolution. These works laid the theoretical foundation for all future work. [6.1]

Turbulence at all scales creates temperature gradients that cause variations in the index of refraction. For smaller scale turbulence (< 100 m length scale), visible and infrared light will have different "optical distances" to travel over fairly short paths. This leads to changes in the phase of the light as shown in Figure 6-5. Phase aberrations, when propagating through space, lead to changes in intensity of the light beam. Small-scale turbulence as it applies to visible and near-IR propagation is typically called "optical turbulence". [6.1]

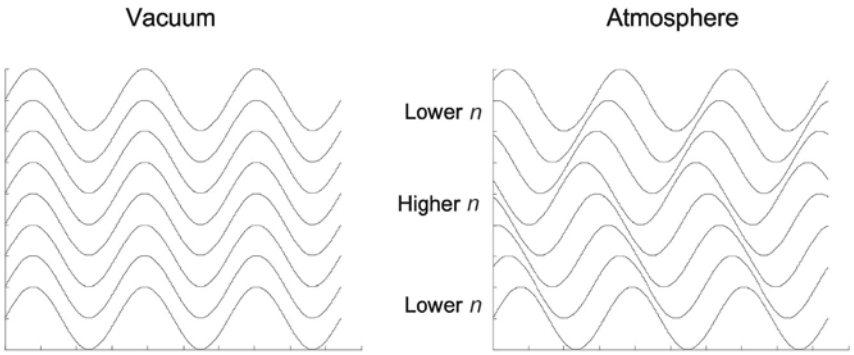

Figure 6-5: Example of how variations in refractive index affect phase of light. Note a lower n implies a faster speed.

Usually, the propagating electromagnetic light wave is represented pictorially by the wavefront, which is the line joining the part of the electromagnetic wave with equal phase. Non-planar wavefronts are called *optical aberrations*. This effect is shown in Figure 6-6. [6.1]

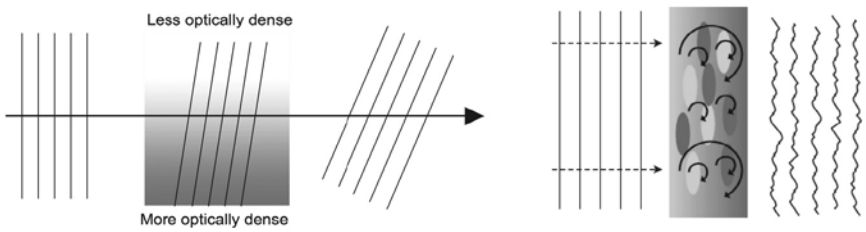

Figure 6-6: Example of how variations in refractive index and turbulence affect the wavefront of electromagnetic energy and create optical distortions or aberrations. [6.1]

For statistical characterizations of small-scale turbulence, it is often assumed the turbulence is isotropic, homogenous, and ergodic. Thus, the statistical behavior remains constant, even with changes in position (homogeneous), direction (isotropic), and time (ergodic). For statistical turbulence, ergodic means that all accessible states are equally probable over a long period of time. Isotopic implies the characterization is independent of direction, and homogeneous defines the turbulence as the same throughout, independent of location. This is shown graphically in Figure 6-7. [6.1]

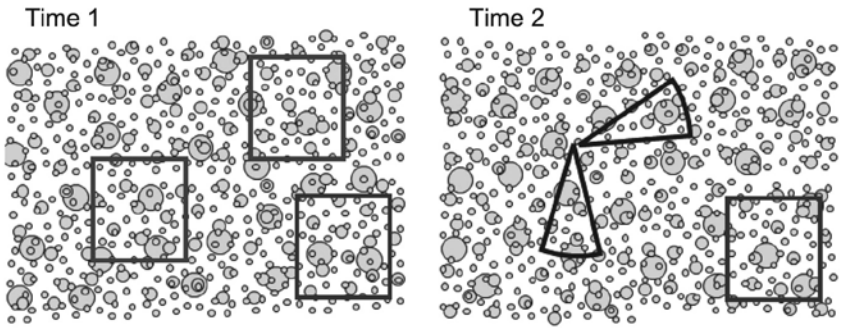

Figure 6-7: Example of sampling a field of turbulence at different positions (square boxes at time 1), in different directions (pie shapes at time 2) and at different times (squares at the lower right at times 1 and 2). [6.1]

Temperature variations are the primary source of refractive index variations. In the visible and near-IR part of the spectrum, this temperature effect can be empirically captured with Equation 6.5.

$$n(T)-1=\left[n(15^{o}C)-1\right]\left[\frac{1.059}{1+\left(0.00366\ {}^{o}C^{-1}\right)T}\right] \tag{6.5}$$

The ergodic/ensemble mean square difference (indicated by the brackets in the two equations below) in the index of refraction at points separated by a distance r, is termed the structure function:

$$D_n(\vec{r}_1,\vec{r}_2)=D_n(r)=\left\langle\left|n(r_1)-n(r_1+r)\right|^2\right\rangle \tag{6.6}$$

Similarly for phase (which defines impact from atmosphere):

$$D_\phi(\vec{r}_1,\vec{r}_2)=D_\phi(r)=\left\langle\left|\phi(r_1)-\phi(r_1+r)\right|^2\right\rangle \tag{6.7}$$

Kolmogorov's theory establishes a structure function for the atmosphere in terms of an index of refraction structure constant, C_n^2, which measures the strength of atmospheric turbulence.

$$D_n(r)=\begin{cases}C_n^2 r^{2/3} & l_0<r<L_0\\ C_n^2 l_0^{-4/3} r^{2/3} & r_0<l_0\end{cases}$$

(6.8)

The index of refraction structure function constant, C_n^2, varies in both time and space. It has been measured at numerous sites and altitudes worldwide and parametric expressions are available. In general, C_n^2 values on the order of 10^{-17} $m^{-2/3}$ and less are considered weak" turbulence and values on the order of 10^{-13} $m^{-2/3}$ and greater are considered "strong" turbulence. [6.1]

The Kolmogorov spectrum is widely used in theoretical calculations. However, it is limited to the inertial subrange, so other models of the turbulence spectrum using refractive index fluctuations are required in some calculations. The inertial subrange is often defined as having an inner scale on the order of 0.1 to 10 mm and an outer scale of 10 s to 100 m, as illustrated in Figure 6.8. [6.1]

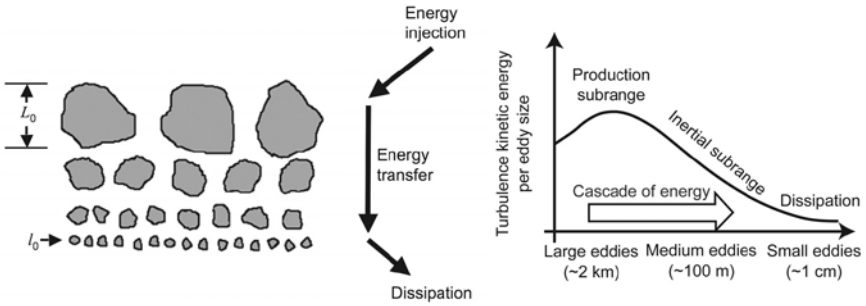

Figure 6-8: Two graphical examples showing how the inertial subrange of turbulence fits between turbulence production at larger scales and viscous energy dissipation at very small scales. Left chart: Inertial subrange in terms of the outer and inner scales and relative eddy size. Right chart: Inertial subrange in terms of relative turbulent kinetic energy. [6.1]

Using Kolmogorov's result, the effect on phase can be written as

$$D_\phi(r) = 2.91k^2 r^{5/3} \int C_n^2 dz \tag{6.9}$$

which is dependent on the path integrated (summed) C_n^2 along the entire path or propagation. The term k in Equation 6.9 is the angular wavenumber, $k = 2\pi/\lambda$. [6.1]

As mentioned above, optical turbulence vertical profiles have been measured at numerous sites worldwide. The optical turbulence database is chiefly derived from thermosonde measurements. Thermosondes are balloon-borne payloads which measure *in-situ* the temperature structure constant (C_T^2) using fine wire probes separated by a one meter horizontal distance. The C_T^2 parameter is measured approximately every seven to eight meters in the vertical. The altitude range of thermosonde measurements is from the surface to 30 km above sea level. Due to solar heating effects on the fine wire probes, thermosonde measurements of C_T^2 are usually made at night. The thermosonde also measures pressure (P), temperature (T), humidity, and horizontal wind velocity using an attached, modified rawinsonde package. Neglecting water vapor effects allows the calculation of the index of refraction structure constant C_n^2 from:

$$C_n^2 = C_T^2 \left[79 \times 10^{-6} \frac{P}{T^2} \right]^2 \qquad (\mathrm{m}^{-2/3}) \tag{6.10}$$

where pressure has units of hectopascals (millibars) and temperature is in K. [6.1]

In general, C_n^2 profiles are highly variable as they often can change two orders of magnitude over very short vertical distances. Typical running mean values (over height) of C_n^2 profiles decrease from maximum values

near the surface to lower values in the mid-troposphere, and then up to a secondary maximum in the vicinity of the tropopause, as shown in Figure 6-9. A number of "standard" C_n^2 profile models have been developed to characterize the average or typical variation of C_n^2 with height. One of the most common is the Hufnagel-Valley model shown in Figure 6.9 (both panels). [6.1]

The Hufnagel-Valley model is specified by the following:

$$C_n^2(\mathrm{h}) = 5.94\times10^{-53}\left(\frac{W}{27}\right)^2 \mathrm{h}^{10}e^{-\mathrm{h}/1000} + 2.7\times10^{-16}e^{-\mathrm{h}/1500} + Ae^{-\mathrm{h}/100} \tag{6.11}$$

where in this case h is height in meters, W is the high altitude wind speed, and A is the C_n^2 surface value. Typical values for W and A, respectively, are 21 m s^{-2} and 1.7 x 10^{-14} $m^{-2/3}$; using these values gives the resulting vertical, ground-to-space C_n^2 profile a Fried Coherence length, r_o = 5 cm, and an isoplanatic angle, θ_o = 7 μrad. Thus, this particular Hufnagel-Valley C_n^2 profile is often referred to as Hufnagel-Valley 5/7 or HV 5/7. [6.1]

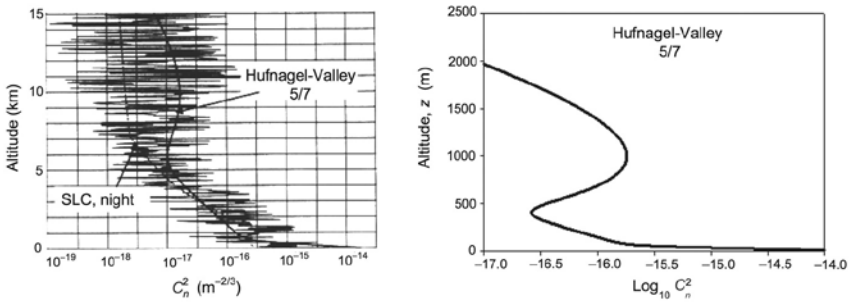

Figure 6-9: Examples of optical turbulence profiles. Left chart: Running means of two standard models overlaid with a single optical turbulence profile measurement from a thermosonde. Right chart: A plot of the Hufnagel-Valley optical turbulence model. [6.1]

The atmosphere reduces laser effectiveness even in fair, cloudless weather due to the attenuating presence of air molecules and aerosols. Optical turbulence causes spatially and temporally varying irradiance patterns, and is present to some degree at all levels of the atmosphere. Degrading atmospheric effects are strongest near the surface within the boundary layer. Some of the degrading effects of the atmosphere can be reduced with a beam control system including adaptive optics. [6.1]

6.2 Adaptive Optics

(U) Adaptive optics (AO) within HEL systems consist of a beacon, a wavefront sensor (WFS), a reconstructor, a deformable mirror (DM) and a control law. We note that the moniker, 'Adaptive Optics' is not to be confused with Adaptive Control. The latter deals with the design of non-linear control algorithms. The control designs of adaptive optics systems, to date, have been mostly limited to linear design methods. However, recent studies show significant improvement with an accompanying non-linear control, adaptive feed-forward loop. The presentation here is limited to the application of linear control theory for a standard adaptive optics loop. The basic components of AO system are sketched in Figure 6-10. [6.1]

6.2.1 Laser Beacon

(U) Adaptive Optics will normally use a beacon as the sensed signal for correction. In 1982, Dr. Julius Feinlieb first proposed the use of a laser beacon for AO, now called an *artificial guide star*. He suggested using the backscatter from a laser beacon focused within the atmosphere. This is called a Rayleigh beacon

since it is formed by the Rayleigh backscatter of the atmosphere. This improvement eliminated the need for a bright object within the field-of-view and essentially opened up the entire sky for compensated viewing. In general, if the image being observed is corrected for the atmospheric path, then the HEL following the same path will be corrected. The Rayleigh beacon is common among astronomical sites and would be used in a ground based LWS. A Rayleigh beacon is limited in height (< 20km) due to the reduction in returned light from the upper atmosphere. Astronomers are now augmenting their Rayleigh beacon AO systems with a sodium laser beacon formed with the 90 km sodium layer. [6.1]

Since a single Rayleigh beacon only samples a portion of the atmosphere affecting image formation it is degraded by Focus Anisoplanatism. This limitation can be avoided if the beacon is focused in the plane of the target. For many laser weapon system (LWS) targets this is the case. See Figure 6-10. The approach uses the diffuse reflectance of the laser beacon off of the target which may provide a higher level of signal than Rayleigh scattering.

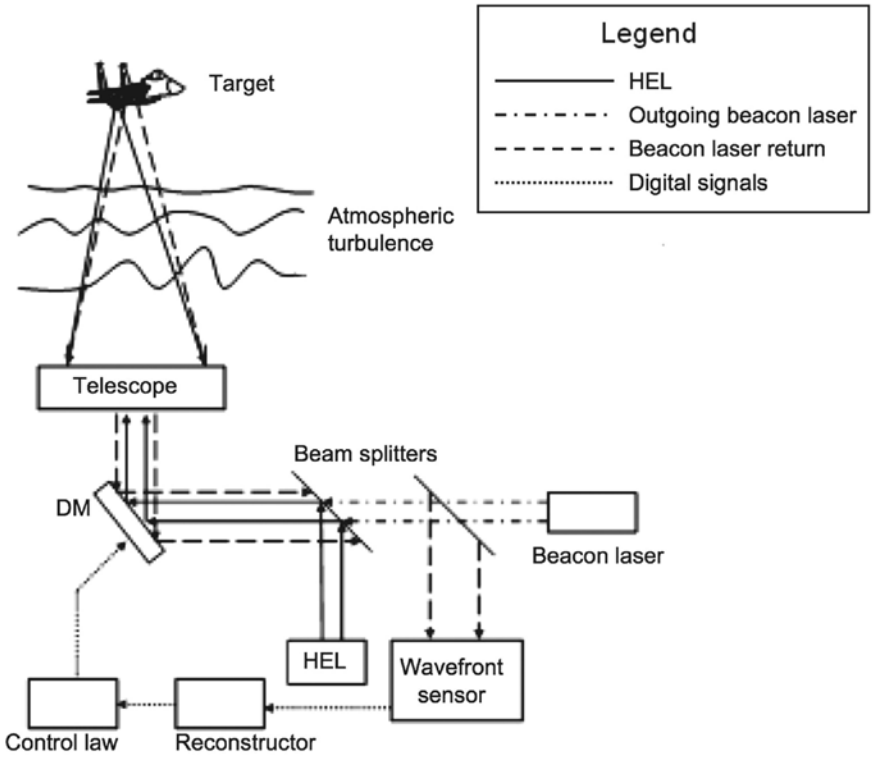

Figure 6-10: The components of an AO subsystem: a WFS, reconstructor, DM, and control law. The WFS measures the atmospheric effects by measuring slopes over an array of subapertures. The reconstructor links the array of slope measurements into a correcting wavefront. The Control Law amplifies the correcting wavefront for error rejection bandwidth and outputs the result to the DM actuator array. The actuators displace the DM mirror faceplate and correct the incoming the wavefront. [6.1]

Usually the laser beacon shares the same aperture that is being compensated. This requires a pulsed laser to time multiplex the outgoing pulse and the sensing of the return. [6.1]

6.2.2 Wavefront Sensor

The depiction in Figure 6-11 is the front end of the most commonly used WFS called a *Shack-Hartmann*. In a Shack-Hartmann WFS design, the wavefront can be well estimated by measuring an array of slopes over

the pupil and then linking them together for a full wavefront estimate. The Shack-Hartmann wavefront sensor consists of a rectangular array of lenses, called a *lenslet* array, and a focal plane array (FPA). With the telescope's entrance pupil relayed onto the lenslet array we can inscribe the image of the clear aperture of the telescope over the lenslet array. The bundle of light that each lenslet intercepts is associated with an area in the telescopes entrance pupil which we call a *subaperture*. The Shack-Hartmann designer attempts to set the size of the subaperture to the smallest r_o expected during operation. This supports the assumption that the portion of wavefront measured by each lenslet is well modeled by its phase slope alone. A one dimensional analog is to use piecewise-linear segments to fit a continuous function. Behind each lenslet is an associated group of pixels of the FPA that measures the spot displacement from nominal. Typically, the nominal location is set with a full aperture plane wave during calibration. Just as we saw in the tracker sensor, the *x*, *y* displacements of each lenslet spot is linearly related to the wavefront's slope over the lenslet. [6.1]

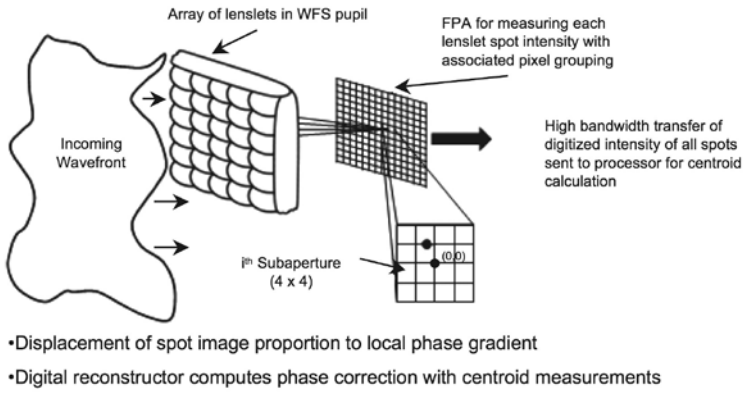

Figure 6-11: Shack-Hartmann WFS lenslet and detector arrays. [6.1]

6.2.3 The Reconstructor

The measurements made by the Shack-Hartmann WFS are the *x* and *y* slopes over each subaperture. The subaperture measurements are linked by the reconstructor to convert the array of slope measurements into a full wavefront phase correction for the DM actuators. The best way to understand how one can accomplish this is to start with the model of the DM. We assume that the response of the DM is linear in actuator displacements. This can be written as

$$\overrightarrow{S_{slp}} = \Gamma_{DM}\overrightarrow{\phi_{act}} \tag{6.12}$$

where:

$\vec{S}_{slp}$ is a vector of slope measurements (λ-waves of tilt);
Γ_{DM} is a matrix defining the linear response of the DM (λ/m);
$\vec{\phi}_{act}$ is the vector of actuator displacements (m).

The elements of Γ_{DM} are constructed using a first-order response of the DM's faceplate (mirror). We define Γ_{DM} with reference to a commonly used alignment between the DM actuators and the subapertures of the WFS called the *Fried geometry*. [6.1]

6.2.4 Deformable Mirrors

The basic function of the DM is to apply a *conjugate* correction to the wavefront. The operation of conjugation is presented with the aid of Figure 6-12. Referencing the top-left of Figure 6-12, assume a plane

wave is transmitted through an unknown aberrator, here depicted as a simple phase delay near the center of the wavefront. As the wave travels through the aberrator, that portion of the wave is delayed with respect to its wings. If no correction is applied, the reflected wave returns with the wings still leading the propagation and the delayed portion is again delayed to twice the aberration (top-right Figure 6-12). In the bottom of Figure 6-12, the wavefront is corrected by placing the same aberration on the DM with the same magnitude. The wings must travel twice the magnitude of the correction for a full reversal of the wavefront - once to the DM, and once after reflection by the DM. This doubling of the DM displacement causes the delayed portion to advance twice the amount of the aberration, but in vector addition. Thus, the return looks identical to the incident, but with a sign reversal in direction. Now as the corrected wavefront returns through the aberrator, the leading portion of the wavefront will be cancelled by the delay of the aberrator and emerge in phase with the wings. The action of forming the return wave identical to the incident, but with a sign change in direction, is called, *conjugation*. Thus, the operation of the DM is to form the conjugate waveform upon reflection. [6.1]

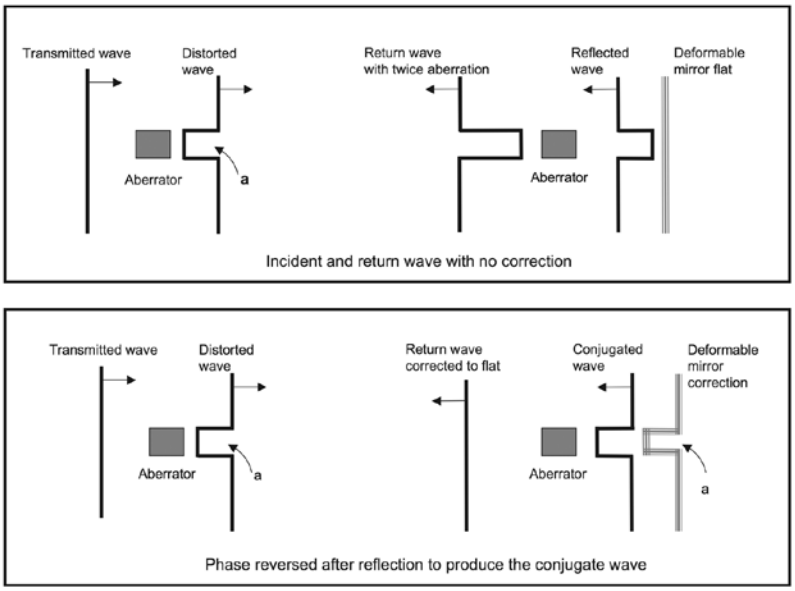

Figure 6-12: Reflected wavefront with and without correction. Reflection of the wavefront, shown at the top of the figure, causes a doubling of the aberration as the wave returns through the aberrator. Applying the conjugate of the aberrated wavefront on the DM causes the wavefront to be corrected as it passes through the aberrator the second time. [6.1]

The above presentation explains the basics of a DM conjugating a wavefront. In the actual AO system the WFS senses the image of the beacon after reflecting off of the DM. Any difference from a well formed spot is sensed and a correction sent to adjust the DM. The outgoing HEL is a near plane wave before reflection off of the DM. Upon reflection it is deformed to have the conjugate of the aberrations sensed on the beacon image. As the HEL propagates through the atmosphere, it undoes the measured effect and returns it a well-focused beam. [6.1]

Various designs of DM's available today include continuous and segmented mirrors. Figure 6-13 show sketches of the three types. The piston-only and piston with tilt designs are available in miniature size using microelectromechanical system (MEMS) technology. The piston-only design is appropriate when many actuators across the aperture are available to provide a good fit to the wavefront with piston-only control elements. [6.1]

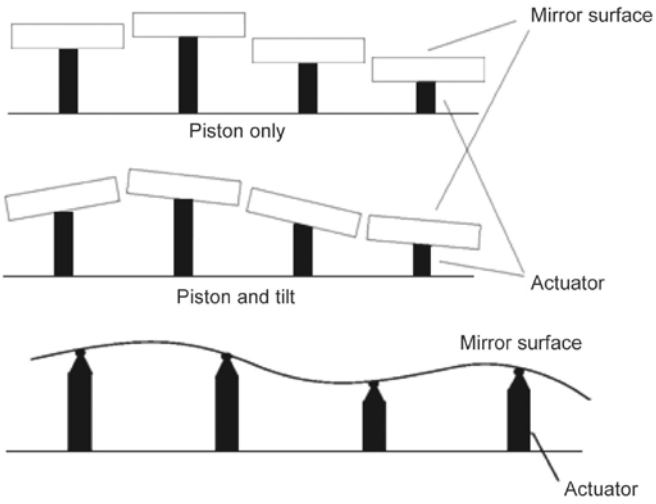

Figure 6-13: Alternate schemes for DM actuation. [6.1]

6.2.5 Adaptive Optics Control Loop

The control block diagram for an adaptive optics loop is shown in Figure 6-14. The reader will recognize the similarity between a DM loop control structure and that used for the tracker. The methods for manipulation and calculation of the transfer functions are similar as well, with one caveat. The DM block diagram represents a multi-input, multi-output (MIMO) system. Thus, each transfer function is actually a matrix of transfer functions and, in general, the matrices do not commute. For comparison, typical tracker control loops utilize a single input, single output (SISO) system. The control theory applied in MIMO-type systems is more complex and less intuitive than that of a SISO system. The concept of gain margin and phase margin lose meaning due to the multiple coupling paths of the matrix formulations. However, given the aligned WFS-DM case with N-actuators, the AO control problem separates into N-SISO control loops. [6.1]

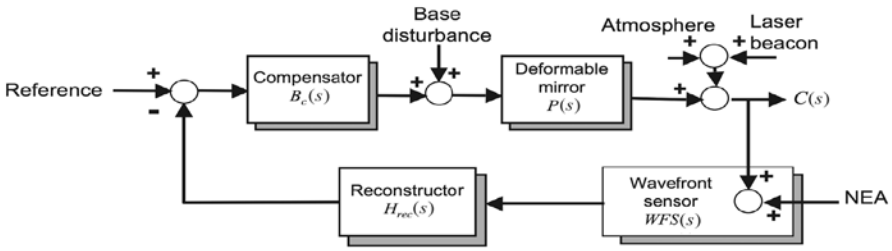

Figure 6-14: Block diagram for an AO control loop. [6.1]

6.3 Summary and Scenario Discussion

The combined and fully correlated atmospheric effects of turbulence, absorption, scattering and thermal blooming on various HEL systems employed in the Black Forest or Persian Gulf regions (or anywhere else in the world) can be explored using an analysis tool called 4-D Weather Cubes. Furthermore, if a suitable HEL propagation code is chosen for use in the Weather Cube computations, the effectiveness of AO to improve HEL system performance in various locations and weather conditions can be quantified.

6.3.1 4D Weather Cubes for Persian Gulf and Black Forest Scenarios

Weather Cubes, anchored to LEEDR, a radiative transfer and atmospheric characterization tool, and

numerical weather prediction (NWP) data, provide expansive data arrays of spatial and temporal variations of meteorological and environmental data that demonstrate how clouds, precipitation, and aerosol haze affect ultraviolet through radio frequency radiative (light) propagation. Furthermore, Weather Cubes always create correlated atmospheric parameters that have actually occurred or might occur together because they are based on actual observations or state-of-the-art scientific predictions of those atmospheric conditions. [6.4]

Weather cubes use LEEDR turbulence (C_n^2) profile calculations and radiative transfer (extinction, transmission, and radiance) with NWP model pressure, temperature, humidity, and wind vector volumetric definitions. HEL system performance statistics are generated when weather cubes are coupled with a propagation code (e.g. HELEEOS which can assess HEL performance with and without AO), allowing for performance binning and percentiles analyses for a variety of engagements that consider spatial and temporal variations in atmospheric conditions. [6.5]

Location	HEL Designation	λ (μm)	Ap Diam (m)	Power (kW)	BQ	Platform Jitter (rad)	Platform Alt (m)	Platform Speed (m/s)	Platform Hdg (deg)	Platform Az (deg)	Target Alt (m)	Range (km)	Target Speed (m/s)	Target Hdg (deg)
Persian Gulf	CUAS	1.06	0.4	50/100/150	2	3.E-06	15	10	75	70	200	5	40	250

Location	HEL Designation	λ (μm)	Ap Diam (m)	Power (kW)	BQ	Platform Jitter (rad)	Platform Alt (m)	Platform Speed (m/s)	Platform Hdg (deg)	Platform Az (deg)	Target Alt (m)	Range (km)	Target Speed (m/s)	Target Hdg (deg)
	IED	1.07	0.15	3/5/10	1.5	2.E-06	3	0	0	0	0	0.1	0	0
Platoon/Patrol	CUAS	1.07	0.3	10/30/50	1.5	2.E-06	3	0	0	240	50	1.7	10	50
Black Forest	CRAM	1.07	0.3	10/30/50	1.5	2.E-06	3	0	0	120	900	1.7	100	300

Figure 6-15: Excel spreadsheet system and engagement specifications inputs for Weather Cube analysis of the Persian Gulf and Black Forest scenarios.

The Persian Gulf and Black Forest scenarios were investigated with Weather Cubes using the system and engagement parameters outlined in Figure 6-15. The Weather Cubes in this study utilized nearly 11 years (2007-2017) of US Global Forecasting System (GFS) NWP data at each of the four forecast cycles per day. This resulted in the performance modelling and statistical compilation of over 15,000 HEL engagements for the twelve different sets of system specifications and geometries shown in Figure 6-15. Histograms of modelled peak irradiance delivered to target performance for two of the twelve engagement scenarios are shown in Figure 6-16.

6.3.2 Discussion of Persian Gulf and Black Forest Scenario Results and Differences

Results of the three Persian Gulf and nine Black Forest engagements clearly demonstrated the effects of absorption, scattering, thermal blooming, and turbulence—especially in terms of range. The best performance and highest peak irradiances delivered were for the lowest power HEL engagements with the IED targets (see right plot in Figure 6-16); this is primarily due to the very short range of only 100 m. The Persian Gulf engagements were modelled with the highest powered (but lowest beam quality) HELs, yet yielded only modest peak irradiances delivered due to those three scenarios having the longest range of 5 km. All scenarios are low altitude and near surface, thus turbulence is a significant deleterious effect for all except the 100 m range IED engagements. Thermal blooming likely affected the CUAS Black Forest engagements given the range and slow target speed. AO (not modelled in these cases) may have improved the performance in the Black Forest CRAM and Persian Gulf CUAS engagements, although AO improvement would be hindered in the Persian Gulf cases due to the laser beam quality of 2.

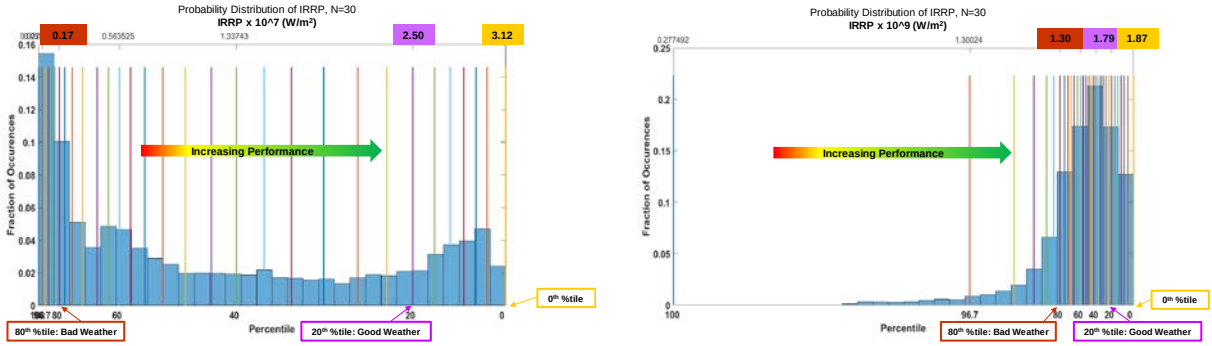

Figure 6-16: Example Weather Cube performance histogram plots for the Persian Gulf 50 kW CUAS (left plot) and the Black Forest 3 kW IED (right plot) engagements. Color-coded values shown at the top of each plot are peak irradiance (IRRP) delivered at the 80th, 20th percentiles and highest values for the engagement in the 15,000+ cases investigated. Note that the peak irradiance values are in units of 1e7 W m^{-2} on the left and 1e9 W m^{-2} on the right.

REFERENCES:

[6.1] Perram, G.P., S.J. Cusumano, R.L. Hengehold, and S.T. Fiorino, 2010: *An Introduction to Laser Weapon Systems*. Directed Energy Professional Society. 463 pp.

[6.2] Fiorino, S.T., R.M. Randall, M.F. Via, and J.L. Burley, 2014: "Validation of a UV-to-RF high-spectral-resolution atmospheric boundary layer characterization tool" *J. Appl. Meteor. Climatol.* Vol 53, No. 1, pp. 136-156.

[6.3] Burley, J.L., S.T. Fiorino, B. Elmore, and J. Schmidt, 2017: "A Fast Calculating Two-Stream-Like Multiple Scattering Algorithm that Captures Azimuthal and Elevation Variations" *J. Appl. Meteor. Climatol.* 56:11, pp. 3049-3063.

[6.4] Schmidt J., J. Burley, B. Elmore, S. Fiorino, K. Keefer, and N. Van Zandt, 2018: "4D Weather Cubes and defense applications" Chapter 14 in *Defense Innovation Handbook*, Badiru & Barlow eds, CRC press, 432 pp.

[6.5] Fiorino, S.T, S.R. Bose-Pillai, J.E. Schmidt, B.J. Elmore, K.J. Keefer, 2020: "Implications of 4D weather cubes for improved cloud free line of sight assessments of free space optical communications link performance," *Opt. Eng.* 59(8), 081808.